
This copy is for your personal, non-commercial use only.

If you wish to distribute this article to others, you can order high-quality copies for your colleagues, clients, or customers by [clicking here](#).

Permission to republish or repurpose articles or portions of articles can be obtained by following the guidelines [here](#).

The following resources related to this article are available online at www.sciencemag.org (this information is current as of November 3, 2014):

Updated information and services, including high-resolution figures, can be found in the online version of this article at:

<http://www.sciencemag.org/content/339/6126/1416.full.html>

Supporting Online Material can be found at:

<http://www.sciencemag.org/content/suppl/2013/03/20/339.6126.1416.DC1.html>

A list of selected additional articles on the Science Web sites **related to this article** can be found at:

<http://www.sciencemag.org/content/339/6126/1416.full.html#related>

This article **cites 43 articles**, 10 of which can be accessed free:

<http://www.sciencemag.org/content/339/6126/1416.full.html#ref-list-1>

This article has been **cited by** 3 articles hosted by HighWire Press; see:

<http://www.sciencemag.org/content/339/6126/1416.full.html#related-urls>

This article appears in the following **subject collections**:

Geochemistry, Geophysics

http://www.sciencemag.org/cgi/collection/geochem_phys

Simple Scaling of Catastrophic Landslide Dynamics

Göran Ekström* and Colin P. Stark

Catastrophic landslides involve the acceleration and deceleration of millions of tons of rock and debris in response to the forces of gravity and dissipation. Their unpredictability and frequent location in remote areas have made observations of their dynamics rare. Through real-time detection and inverse modeling of teleseismic data, we show that landslide dynamics are primarily determined by the length scale of the source mass. When combined with geometric constraints from satellite imagery, the seismically determined landslide force histories yield estimates of landslide duration, momenta, potential energy loss, mass, and runout trajectory. Measurements of these dynamical properties for 29 teleseismogenic landslides are consistent with a simple acceleration model in which height drop and rupture depth scale with the length of the failing slope.

Seismic radiation from landslides is broadband and complex (1). Short-period waves result from the myriad momentum exchanges taking place within the granular mass and along its sliding boundary. They are distributed in time and low in amplitude compared with the impulsive radiation associated with the sudden stress drop in tectonic earthquakes. Long-period waves radiated by landslides are simpler: They are generated by the broad cycle of unloading and re-loading of the solid Earth (2–4) induced by the bulk acceleration and deceleration of the landslide mass. The corresponding momentum exchange is complicated by entrainment and deposition (5–7) during motion and by topographic undulations along the slide path (8). Characteristic unloading-reloading times in large landslides are several tens of seconds, making them efficient sources of seismic waves at periods of that order (9).

Traditional earthquake monitoring conducted by national and international agencies is designed for detection of impulsive short-period seismic waves and for location of associated tectonic earthquakes and explosions. Landslide detections are rare. A complementary method based on near-real-time data from the Global Seismographic Network (GSN) allows for the detection of seis-

mic events through continuous back-projection of the long-period wavefield (10–12). This event-detection algorithm detects >90% of magnitude $M \geq 5.0$ shallow earthquakes reported by other agencies and identifies about 10 events each month that are not in other seismicity catalogs. Some of these unassociated events have been correlated with large-scale glacier calving (13, 14) and volcanic unrest (15). Here, we identify and investigate another subset of these events associated with catastrophic (large and fast) landslides.

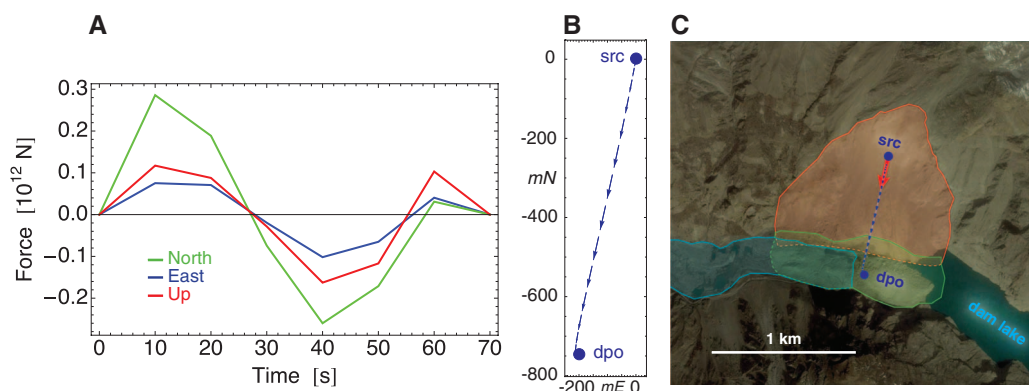
The event-detection algorithm locates events with an initial accuracy of 20 to 100 km (10). A terrestrial landslide source is established by combining this geographic location with satellite imagery, field photographs, news reports, local seismic recordings, and other sources. A comprehensive investigation of 195 unassociated detections for 2010 led to the identification of 11 major landslides (table S1, events 16 to 26). All of the seismically detected landslides generated long-period surface waves (SW) roughly equivalent to a magnitude $M_{SW} \sim 5$ tectonic earthquake, and all were recorded at multiple seismographic stations. Tectonically generated surface-wave signals of this magnitude are routinely used to determine earthquake fault geometries and seismic moments (16), suggesting that similar methods could also be used to provide a quantitative characterization of the detected landslides. For example, Kanamori and co-workers (17, 18) measured a subhorizon-

tal force of ~ 150 s duration and maximum amplitude $\sim 10^{13}$ N associated with the massive debris avalanche after the 1980 eruption of Mount St. Helens volcano (table S1). Seismological analyses of long-period data have usually focused on single landslide events and typically have been limited to estimation of the average slide direction (often only in the horizontal), peak force, and duration of sliding (19–22). Field observations, by contrast, frequently suggest complex three-dimensional (3D) landslide trajectories, and numerical modeling has highlighted the effects of such complexity on the radiated seismic waves (7, 8).

We developed an inverse method (12) to infer the 3D force sequence generated by bulk landslide motion (23)—from which we can deduce the trajectory of slip and dynamic properties. The new algorithm builds on and extends established methods used in earthquake analysis (12, 16). When applied to one of the largest landslides of 2010, this approach results in a first-order characterization of the event (Fig. 1). On 4 January of that year, our algorithm (10, 11) automatically detected a seismic event of long-period magnitude $M_{SW} \approx 5.3$ at 08:36 GMT and roughly located the source in northern Pakistan (table S1). None of the international earthquake-monitoring agencies ISC, IDC, or NEIC reported this event. After anecdotal reports that a major landslide had struck the village of Attabad that morning—blocking the Karakoram Highway, damming the Hunza River, and causing several fatalities (24)—we inspected long-period waveform data recorded on proximal stations and established that the seismic signal was likely caused by the Attabad slope failure. This association was confirmed by our inverse model, which provided a more accurate source location within 15 km of Attabad and which pointed to a direction of motion down to the south-southwest, consistent with local reports. These reports also indicated a time of failure consistent with the seismic detection.

The estimated time sequence of forces induced by acceleration of the Hunza-Attabad landslide indicates a roughly sinusoidal sequence lasting $\Delta t \sim 60$ s (Fig. 1A). The 3D force vector components vary in a synchronous fashion, which suggests a consistent azimuth of acceleration and

Fig. 1. Landslide force history and trajectory for the Hunza-Attabad landslide. **(A)** Inversion of the landslide force history $\mathbf{F}(t)$ (LFH) of this event, pinning the time of main failure at 08:37 UT (table S1). **(B)** The planform trajectory of landslide motion deduced by doubly integrating the LFH and scaling by the runout distance mapped in (C). **(C)** Satellite-image mapping of the landslide scar and runout. The estimated centers of the source (“src”) and deposits (“dpo”) are indicated; their spatial separation was used to estimate D_{hr} , determine the effective mass, and scale the displacement trajectory $\mathbf{D}(t)$.



Lamont-Doherty Earth Observatory of Columbia University, Palisades, NY 10964, USA.

*Corresponding author. E-mail: ekstrom@ldeo.columbia.edu

deceleration and therefore a linear runout. During the first 25 s the force vector points consistently to the north-northeast with an upward vertical component, indicating reaction to acceleration of the slide mass downhill in the south-southwest direction. The subsequent time series reflects reversal of the force vector during deceleration, as the slide mass approached the bottom of the valley.

Because the negated force history is equivalent to the rate of change of bulk landslide momentum over time (23), its integration gives the

bulk momentum over time $\mathbf{p}(t) = (m\mathbf{v})(t)$. This time series is constrained to be stationary during inversion. Assuming a constant bulk mass m over time, further integration gives the mass-scaled, 3D vector trajectory of motion $m\mathbf{D}(t)$. If an independent measure of landslide volume or mass m is available, we can divide by m to obtain the 3D runout $\mathbf{D}(t)$ and compare it against terrain data and postfailure imagery to test the validity of the inversion results and the assumption of constant mass. Alternative-

ly, we can estimate the bulk landslide mass by comparing the mass-scaled maximum horizontal displacement mD_h with a center-of-mass displacement estimated from terrain data and imagery. Using the second approach, illustrated in satellite imagery of Hunza-Attabad (Fig. 1C), we estimated a horizontal center-of-mass displacement of 940 m, which gave a mass of $m \approx 1.4 \times 10^{11}$ kg and the runout path $\mathbf{D}(t)$ shown in Fig. 1B. Evaluation in the field has estimated the deposited volume at ~ 45 million m^3 (24). Assuming a debris

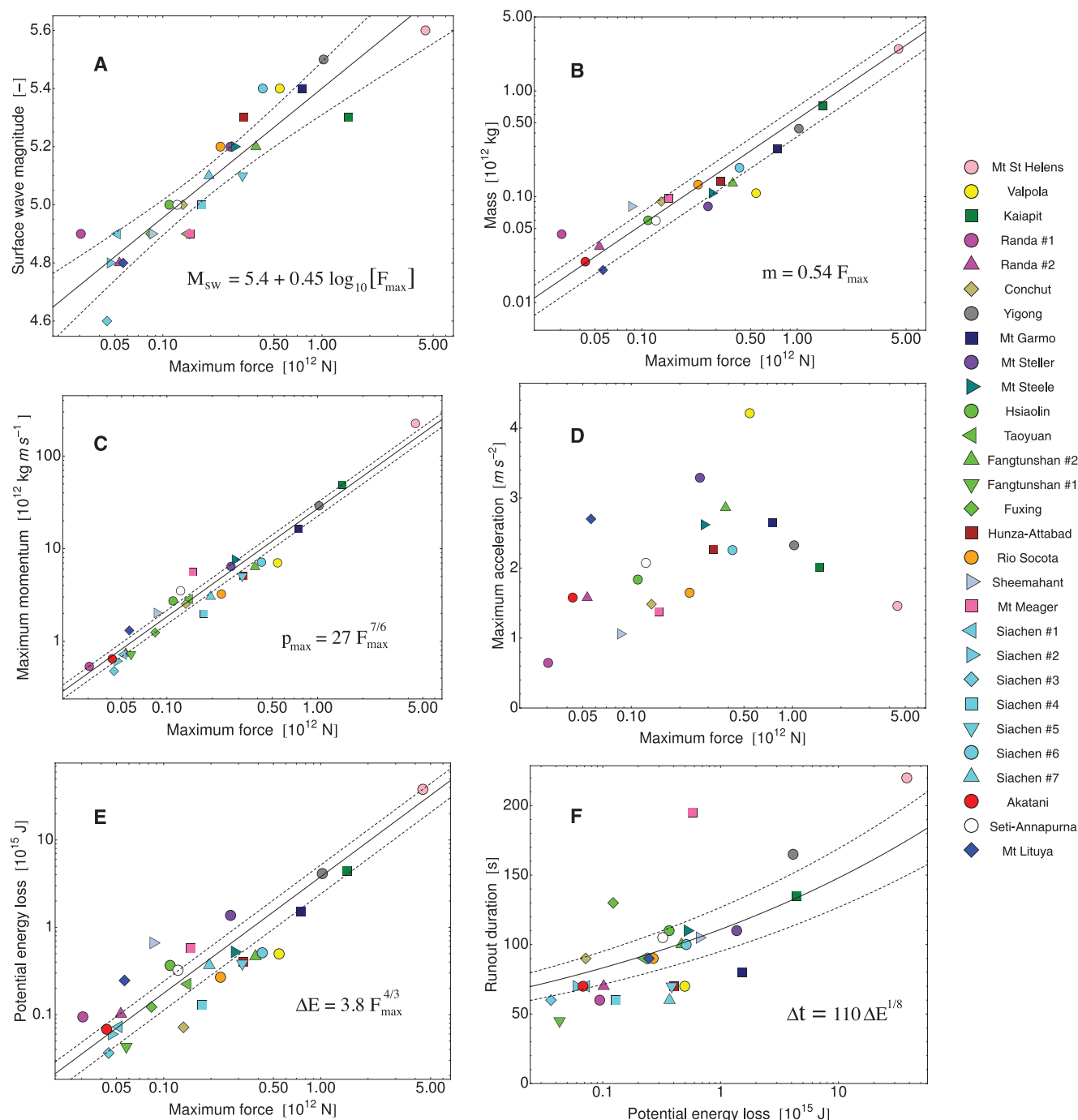


Fig. 2. Maximum force F_{\max} versus (A) long-period surface-wave magnitude M_{SW} , (B) mass m , (C) maximum momentum p_{\max} , (D) maximum acceleration a_{\max} , and (E) potential energy loss ΔE . Runout duration Δt versus potential

energy loss ΔE is shown in (F). In (A) to (C), (E), and (F), the solid lines show model fits and the dashed lines indicate model mean confidence intervals at the 99% level.

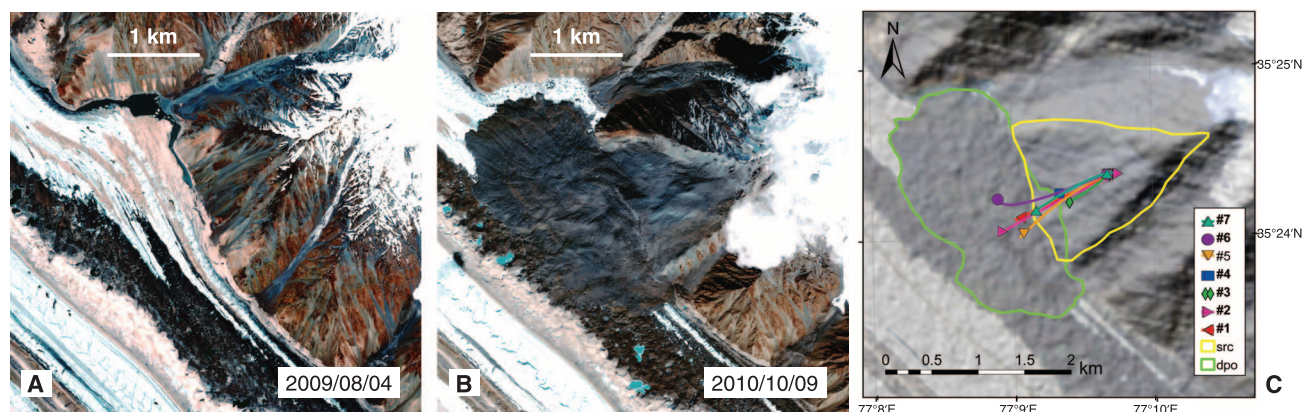


Fig. 3. Siachen landslides, September 2010. **(A)** Pre- and **(B)** postevent GeoEye 50-cm-resolution visible and near-infrared imagery of Siachen Glacier landslide complex. **(C)** Inferred trajectories for the seven Siachen landslides. The slide origins were

chosen to coincide, in order to illustrate the good agreement in average slide direction, with some variability in motion in the lower portions of the trajectories. Outlined in green and yellow are the approximate source and deposit areas, respectively.

density of 2400 kg m^{-3} , this suggests a source mass of $\sim 1.1 \times 10^{11} \text{ kg}$, broadly consistent with our estimate.

We applied the technique of landslide seismic detection and source inversion to a total of 29 events spanning 1980–2012 (table S1). This set includes the three largest landslides of the last 33 years: Mount St. Helens in 1980 (table S1), Kaiapit in 1988 (25), and Yigong in 2000 (26). Of these 29 events, 27 were recorded on global network stations and the two smallest—at Fāngtúnshān/Tāimā in Taiwan (27) in 2009 and Akatani in Japan (28) in 2011—were well recorded on regional networks. By analyzing all 29 landslides in a methodologically consistent fashion, we generated empirical constraints on catastrophic landslide dynamics spanning three orders of magnitude of failure mass that can be used with confidence in analyses of scaling (tables S1 and Fig. 2).

A practical result is the logarithmic relationship (Fig. 2A) that we see between the long-period magnitude M_{SW} and the maximum force F_{max} . The magnitude estimates span $M_{\text{SW}} \approx 4.6$ to 5.6 and are available only for the 27 global detections. The maximum forces here span $F_{\text{max}} \approx 4 \times 10^{10}$ to $5 \times 10^{12} \text{ N}$ and are typically associated with the acceleration phase of the landslide. The correlation is strong, suggesting that the maximum force can be estimated from the long-period magnitude alone (to within a factor of 2) and prior to waveform modeling.

We find a consistent pattern of scaling (Fig. 2, B to F) among the inferred dynamic properties that can be explained with a very simple model of slope collapse and acceleration in which a single length scale L determines all the geometrical properties of the landslide source and its acceleration phase (12). The simple model and the inversion results indicate a linear dependence of landslide mass on maximum force $m \approx 0.54 F_{\text{max}}$ (Fig. 2B). They indicate no scaling dependence, but much variability (Fig. 2D), for peak acceleration $a \approx 2 \text{ m s}^{-2}$. Observed scaling dependencies on maximum force match model deductions: Peak momentum is $p_{\text{max}} \approx 27 F_{\text{max}}^{7/6}$ (Fig. 2C), potential energy loss is $\Delta E \approx 3.8 F_{\text{max}}^{4/3}$

(Fig. 2E), and runout duration is $\Delta t \approx 127 F_{\text{max}}^{1/6}$. Similarly, we find dependencies on potential energy loss such as $\Delta t \approx 110 \Delta E^{1/8}$ (Fig. 2F) and $p_{\text{max}} \approx 10 \Delta E^{7/8}$ that accord with the model. Together our results indicate peak kinetic energy is on average about 24% of potential energy loss.

A practical outcome is that the mass-force relation can be combined with the observed scaling between magnitude and force to provide an approximate means of estimating landslide mass (in 10^{12} kg) from long-period magnitude alone as $m \approx 0.54 \times 10^{2.2 M_{\text{SW}} - 12}$.

Runout duration Δt and trajectory $\mathbf{D}(t)$ inferred seismically reflect the phase of major height drop and thus large force. For some landslides, however, particularly for those running onto and down glaciers [such as Mount Garmo (29) in 2001 and Mount Lituya in 2012], a second, longer phase of low gradient, likely low-deceleration runout, was mapped on imagery, but not recorded in the long-period seismicity. Such long-runout events likely indicate unusually low rates of energy dissipation as a result of frictional melting of glacial ice.

The most notable, previously undocumented landslides we identified are the seven catastrophic (M_{SW} 4.6 to 5.4; table S1) events detected over 4 days in September 2010 and located in the eastern Karakoram. All exhibited the seismic characteristics of landslides, and none were detected by earthquake monitoring agencies. Our inversions of these events indicate a common runout direction of west–west-southwest for all the failures, and analysis of multitemporal Landsat imagery (Fig. 3C) identified only one candidate slope failure, collapsing onto the Siachen Glacier, consistent with this time window and geographic location. Subsequent mapping using multitemporal GeoEye imagery (Fig. 3, A and B) confirmed multiple failures of the northern flank of the valley.

Unlike the Mount Garmo and Mount Lituya events, runout over the Siachen glacier surface was relatively short and comparable to the height drop. Using the GeoEye imagery, we estimated runout for the largest event at $D_h \approx 1320 \text{ m}$ and

deduce the failure mass at around $m \approx 1.9 \times 10^{11} \text{ kg}$ and maximum acceleration of 2.2 m s^{-2} . Because the other six events could not be tied to runout patterns in the imagery, we assumed the same maximum acceleration to calibrate their landslide force history (LFH) inversions, yielding estimates of failure masses ranging from $m \approx 1.1 \times 10^{10} \text{ kg}$ to $1.4 \times 10^{11} \text{ kg}$.

This sequence of massive landsliding is an example of progressive slope failure involving multiple collapses of bedrock volumes each exceeding 10^6 to 10^7 m^3 . Although it is recognized that episodes of massive mass-wasting often comprise a hierarchy of individual landslide events, repeated similar-scale failures of the same mountain slope over mere days are more difficult to explain. In our catalog of inversions, only the paired Randa events (30) in 1991 involve closely repeated failure of a similar scale at the same location. Were it not for the seismic detection, force inversion, and satellite-image mapping used here, the Siachen Glacier landslide deposit would likely be falsely interpreted as the composite of one or two extremely large failures. What is more, given its remote location, it would likely have gone undetected for some time.

References and Notes

1. D. Weichert, R. B. Horner, S. G. Evans, *Bull. Seismol. Soc. Am.* **84**, 1523 (1994).
2. Y. Takei, M. Kumazawa, *Geophys. J. Int.* **118**, 20 (1994).
3. Y. Fukao, *Geophys. J. Int.* **122**, 243 (1995).
4. M. J. McSaveney, G. Downes, in *Landslides*, J. Rybar, J. Stemberk, P. Wagner, Eds. (Balkema, Lisse, Netherlands, 2002), pp. 649–654.
5. G. B. Crosta, H. Chen, C. F. Lee, *Geomorphology* **60**, 127 (2004).
6. S. N. Ward, S. Day, *Geophys. J. Int.* **167**, 991 (2006).
7. L. Moretti et al., *Geophys. Res. Lett.* **39**, L16402 (2012).
8. P. Favreau, A. Mangeney, A. Lucas, G. Crosta, F. Bouchut, *Geophys. Res. Lett.* **37**, L15305 (2010).
9. E. A. Okal, *J. Phys. Earth* **38**, 445 (1990).
10. G. Ekström, *Bull. Seismol. Soc. Am.* **96**, (4A), 1201 (2006).
11. G. Ekström, M. Nettles, Global CMT catalog (2012); <http://globalcmt.org>.
12. See supplementary materials on Science Online.
13. G. Ekström, M. Nettles, G. A. Abers, *Science* **302**, 622 (2003).
14. M. Nettles, G. Ekström, *Annu. Rev. Earth Planet. Sci.* **38**, 467 (2010).

15. A. Shuler, G. Ekström, *J. Volcanol. Geotherm. Res.* **181**, 219 (2009).
16. G. Ekström, M. Nettles, A. M. Dziewonski, *Phys. Earth Planet. Inter.* **200-201**, 1 (2012).
17. H. Kanamori, J. W. Given, *J. Geophys. Res.* **87**, 5422 (1982).
18. H. Kanamori, J. W. Given, T. Lay, *J. Geophys. Res.* **89**, 1856 (1984).
19. H. S. Hasegawa, H. Kanamori, *Bull. Seismol. Soc. Am.* **77**, 1984 (1987).
20. E. E. Brodsky, E. Gordeev, H. Kanamori, *Geophys. Res. Lett.* **30**, 2236 (2003).
21. M. La Rocca *et al.*, *Bull. Seismol. Soc. Am.* **94**, 1850 (2004).
22. N. A. Pino, M. Ripepe, G. B. Cimini, *Geophys. Res. Lett.* **31**, L02605 (2004).
23. W. G. Pariseau, *Eng. Geol.* **16**, 111 (1980).
24. D. Petley, *Int. Water Power Dam Constr.* **63**, 27 (2011).
25. M. Peart, *Q. J. Eng. Geol.* **24**, 399 (1991).
26. Y.-J. Shang *et al.*, *Geomorphology* **54**, 225 (2003).
27. C.-H. Lin, H. Kumagai, M. Ando, T.-C. Shin, *Geophys. Res. Lett.* **37**, L22309 (2010).
28. M. Yamada, Y. Matsushi, M. Chigira, J. Mori, *Geophys. Res. Lett.* **39**, L13301 (2012).
29. V. M. Kotlyakov *et al.*, *Mater. Gliatsiologicheskikh Issledovaniy* **95**, 221 (2003).
30. E. Eberhardt, D. Stead, J. S. Coggan, *Int. J. Rock Mech. Min. Sci.* **41**, 69 (2004).

Acknowledgments: We are grateful to C.-W. Lin, R.-J. Rau, S.-P. Lee, Hongey Chen, S.-H. Liu, and Y.-C. Tsang for help with analysis of landslides triggered by Typhoon Morakot; to

E. Choi and M. Reitz for discussions on landslide mechanics; and to D. Petley for help and information on several of the landslide events reported here. Data are available in the supplementary materials. This research was supported by NSF Awards EAR-0824694, EAR-1150072, and EAR-1227083.

Supplementary Materials

www.sciencemag.org/cgi/content/full/339/6126/1416/DC1

Materials and Methods

Supplementary Text

Fig. S1

Table S1

References (31–50)

19 November 2012; accepted 30 January 2013

10.1126/science.1232887

Two Modes of Change in Southern Ocean Productivity Over the Past Million Years

S. L. Jaccard,¹ C. T. Hayes,^{2,5} A. Martínez-García,¹ D. A. Hodell,³ R. F. Anderson,^{2,5} D. M. Sigman,⁴ G. H. Haug¹

Export of organic carbon from surface waters of the Antarctic Zone of the Southern Ocean decreased during the last ice age, coinciding with declining atmospheric carbon dioxide (CO₂) concentrations, signaling reduced exchange of CO₂ between the ocean interior and the atmosphere. In contrast, in the Subantarctic Zone, export production increased into ice ages coinciding with rising dust fluxes, thus suggesting iron fertilization of subantarctic phytoplankton. Here, a new high-resolution productivity record from the Antarctic Zone is compiled with parallel subantarctic data over the past million years. Together, they fit the view that the combination of these two modes of Southern Ocean change determines the temporal structure of the glacial-interglacial atmospheric CO₂ record, including during the interval of “lukewarm” interglacials between 450 and 800 thousand years ago.

Antarctic ice core measurements reveal that regional air temperatures and atmospheric CO₂ concentration (*p*CO₂) were tightly correlated over glacial-interglacial cycles of the past 800 thousand years (ky) (1). Many studies have inferred a dominant role for the Southern Ocean in modulating glacial-interglacial variability of atmospheric *p*CO₂ (2). The central role of the Southern Ocean is thought to reflect its leverage on the global efficiency of the biological pump, in which the production, sinking, and deep remineralization of organic matter sequesters carbon in the ocean interior, lowering atmospheric CO₂. Dense subsurface water masses outcrop in the Southern Ocean, providing exchange pathways between the deep ocean and the atmosphere. Vertical exchange of water causes deeply sequestered CO₂ and nutrients to be mixed to the surface, fueling high rates of phytoplank-

ton productivity. Today, the Southern Ocean is the principal leak in the biological pump, because export production is inadequate to prevent the evasion of deeply sequestered carbon when waters are exposed to the atmosphere. The polar CO₂ leak can be directly inhibited during glacial stages by factors such as increased sea-ice

cover (3) and/or changes in buoyancy forcing and convection (4, 5). In addition, the glacial CO₂ reduction associated with these mechanisms would have been amplified by iron fertilization of the Subantarctic Zone (SAZ) of the Southern Ocean (6, 7) and associated alkalinity feedbacks (8).

Export production records from the Antarctic Zone (AZ) have been used to trace changes in the rate of Southern Ocean overturning through time (9, 10). However, these records only cover the last glacial cycle, restricting our understanding of the evolution of the Antarctic component of this two-mode system by which the Southern Ocean regulates the transfer of carbon between the ocean interior and the atmosphere over previous climatic cycles. Here, we report a high-resolution relative elemental concentration record from Ocean Drilling Program (ODP) site 1094 (53.2°S, 05.1°E; water depth 2850 m) (Fig. 1), which traces changes in AZ export production over the past million years (figs. S1 and S2). The time resolution achieved here rivals the measurement density typical for Antarctic ice-core records. These observations are complemented with reconstruction of ²³⁰Th-normalized biogenic particle flux to the seafloor covering the last two glacial terminations (Fig. 2).

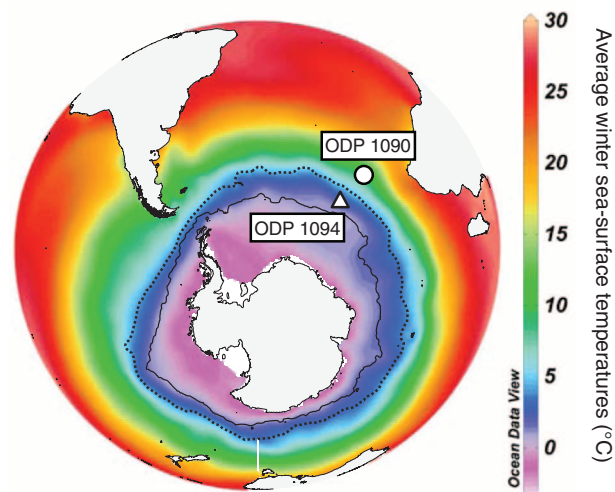


Fig. 1. Core locations shown on the January to March SST field. The black line delineates maximum winter sea-ice extent (using the 90% winter sea-ice concentration line) based on the Hadley Center sea-ice concentration data for 1978 to 2010 (34).

¹Geological Institute, Department of Earth Sciences, ETH Zurich, Zurich, Switzerland. ²Lamont-Doherty Earth Observatory, Columbia University, Palisades, NY, USA. ³Godwin Laboratory for Paleoclimate Research, Department of Earth Sciences, University of Cambridge, Cambridge, UK. ⁴Department of Geosciences, Princeton University, Princeton, NJ, USA. ⁵Department of Earth and Environmental Sciences, Columbia University, New York, NY, USA.

*Corresponding author. E-mail: samuel.jaccard@erdw.ethz.ch